

Extraction of Effective Cement Paste Diffusivities from X-ray Microtomography Scans

M. R. Karim · K. Krabbenhoft

Received: 22 June 2009 / Accepted: 15 November 2009 / Published online: 24 December 2009
© Springer Science+Business Media B.V. 2009

Abstract The problem of extracting effective diffusivities of cement pastes on the basis of X-ray microtomography images is considered. A general computational homogenization framework is developed and applied to a variety of cement pastes whose microstructure has been digitized to a resolution of 1 μm . At this resolution, important submicron features are not resolved. Consequently, we propose a methodology whereby the pore space is ascribed a diffusivity less than the free diffusivity. For this purpose, a simple rule that incorporates microtomography data is proposed and shown to yield satisfactory results.

Keywords Homogenization · Microtomography · XMT · Cement paste · Diffusion · Finite elements

1 Introduction

The transport properties of cement pastes are of crucial importance to the durability of much of our civil infrastructure. Due to its corrosive effects and abundance in many natural environments, considerable efforts have been made to quantify particularly the transport of chloride. To date, most research has been concerned with the diffusive transport through fully saturated cement pastes, and a number of specialized testing methods for evaluating the effective diffusivity have been developed (Andrade 1993; Friedmann et al. 2004; Krabbenhoft and Krabbenhoft 2008; Tang and Nilsson 1992).

As an alternative to traditional experimental determination of transport properties of porous materials, a number of studies have recently demonstrated the feasibility of ‘virtual experiments’. The basic idea here is to obtain detailed three-dimensional images of the microstructure of the material in question. The relevant tests are then simulated, and the

M. R. Karim · K. Krabbenhoft (✉)
Centre for Geotechnical and Materials Modelling, University of Newcastle, Callaghan, NSW, Australia
e-mail: kristian.krabbenhoft@newcastle.edu.au

K. Krabbenhoft
Department of Industrial and Civil Engineering, University of Southern Denmark, Odense, Denmark

quantities of interest, for example, effective diffusion coefficients, are extracted in much the same way as in traditional physical laboratory tests. Typically, the microstructure of the material is assessed using X-ray microtomography (XMT), while the virtual tests are carried out using either finite element/difference analyses or more specialized techniques such as lattice-Boltzman methods and Brownian motion simulations. Representative works combining both elements, i.e. imaging and simulation, include [Bentz et al. \(2000\)](#); [Knackstedt et al. \(2006\)](#); [Koster et al. \(2006\)](#); [Krabbenhoft et al. \(2008\)](#), and [Promentilla et al. \(2008, 2009\)](#).

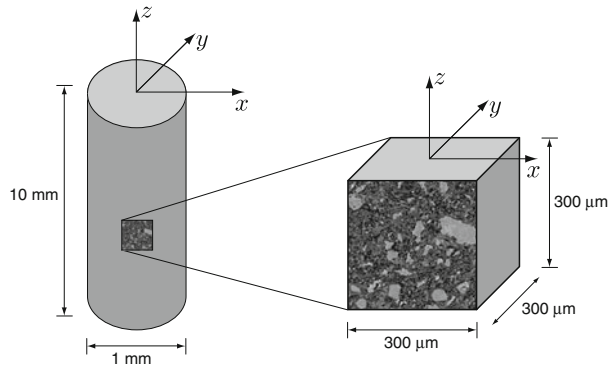
The methodology described above involves a number of significant challenges. First, one has to deal with very large data sets. Thus, digitized material samples consisting of $10^9 - 10^{10}$ voxels (volume pixels) are not uncommon. Regardless of which method of simulation is chosen, it is necessary to pay particular attention to this reality. In the present study where the finite element method is used, specialized iterative solvers for the solution of large systems of linear equations, which at times are severely ill-conditioned, have been developed. Furthermore, to limit the size of the problems solved in the actual simulations, a statistical homogenization procedure has been formulated. The resulting theoretical and computational framework is generally applicable to mass diffusion in porous materials (as well as to heat conduction and related physical phenomena in general heterogeneous materials).

Another, and in many ways more serious, complication with the virtual testing methodology is that important material characteristics below the length scale of the scan resolution may remain unaccounted for. In the present study where XMT images of cement pastes at a resolution of $\approx 1 \mu\text{m}$ are considered, this is very much the case. As will be discussed in detail later on, this level of resolution does not account for submicron features that are of crucial importance to mass diffusion processes. Consequently, it is necessary to make a less sharp distinction between the solid and pore phases than would ideally be desirable. More concretely, we find it necessary to ascribe part of pore space a microscopic diffusion coefficient less than the free diffusion coefficient which would normally be expected to characterize the transport within the individual pores. A new rule that incorporates XMT data has been developed for this purpose.

The approach of not distinguishing sharply between the pore and solid phases has a number of similarities with other recent work, in particular that of [Bentz et al. \(2000\)](#) who obtained microtomographic images of Fontainebleau sandstone and determined effective diffusivities numerically by means of a finite difference method. However, owing to the resolution of the images ($19 \mu\text{m}$, enhanced to $6.65 \mu\text{m}$ by optical magnification), the ‘solid phase’ was not considered impermeable but ascribed a not insignificant microscopic diffusivity. Furthermore, recent work of [Promentilla et al. \(2008, 2009\)](#) on cement pastes scanned at a resolution of $0.5 \mu\text{m}$ shows that it is generally non-trivial to segment the raw grayscale XMT data into solid and pore phases. Moreover, it is demonstrated that the end result, in terms of effective diffusivity, depends strongly on the particular way that the segmentation is carried out. These findings are confirmed by the present study.

In the following, we describe a complete procedure for the extraction of effective diffusion coefficients of digitized cement pastes. First, in [Sect. 2](#), the material and XMT data are described in some detail. In particular, a procedure for segmenting the XMT data is presented, and a number of relevant microstructural correlation functions are discussed. The governing equations are summarized in [Sect. 3](#) along with key results from homogenization theory. Next, in [Sect. 4](#), the necessary computational procedures are described with the numerical results being presented and discussed in [Sect. 5](#). Finally, in [Sect. 6](#), we discuss a means of correcting the images for unresolved submicron features before conclusions are drawn in [Sect. 7](#).

Fig. 1 Experimental setup: cylindrical sample used in the micro-CT scanning (*left*) and extracted $300\ \mu\text{m}^3$ digitized volume used in the virtual tests (*right*)



2 Materials and XMT Data

For the present study, the NIST Visible Cement Data Set (Bentz et al., 2002) was used. This data set contains images of cement pastes with different water/cement ratios and at various stages of hydration. In order to illustrate the procedures developed, in the following we will use a particular data set which describes the microstructure of a cement paste with an initial water/cement ratio of $w/c = 0.45$ and a hydration time of 137 h.

The cement was prepared according to standard specifications as described by Bentz et al. (2002). After drill mixing in a plastic beaker, small parts of the paste were ‘extruded’ into circular tube molds with an internal diameter of 1 mm (see Fig. 1). Subsequently, the whole assembly was scanned at a resolution of $0.95\ \mu\text{m}$, and reconstructed three-dimensional data sets containing $1024 \times 1024 \times 1024$ voxels (volume pixels) were obtained. From these data sets, smaller volumes consisting of 300^3 voxels were extracted. These data form the basis of the virtual testing conducted in the present study. Regarding the rather unusual extrusion of the cement pastes into the thin tube molds, it is possible that a certain amount of anisotropy may have been induced. Indeed, this is what our results indicate as will be discussed in detail in the following sections. For this reason, we introduce the principal axes as shown in Fig. 1. The cylinder axis is denoted by z , whereas two arbitrarily chosen orthogonal directions perpendicular to the z -axis are denoted by x and y , respectively.

2.1 Data Segmentation

Standard XMT images comprise grayscale maps with values proportional to the linear attenuation coefficient at each material point. Typically, the data is organized as a collection of cubic volume elements (voxels), each of which is assigned a unique grayscale value. Next, the data are segmented into a number of distinct categories corresponding to distinct material phases. For cement paste, the most basic distinction is between solids and pores (air or water filled). A further subdivision of the solid phase into hydrated and unhydrated cement could also be considered.

Any segmentation scheme involves a number of subjective decisions, and a large literature exists on the general subject of image segmentation (Pal and Pal (1993, see e.g. the review of)). In the present study, the basic problem can be reduced to determine a threshold below which the voxels are deemed to belong to the pore space and above which they are part of the solid phase. For the purpose of determining this threshold, it is useful to consider the frequency distribution of the grayscale count. This distribution is shown in Fig. 2. From

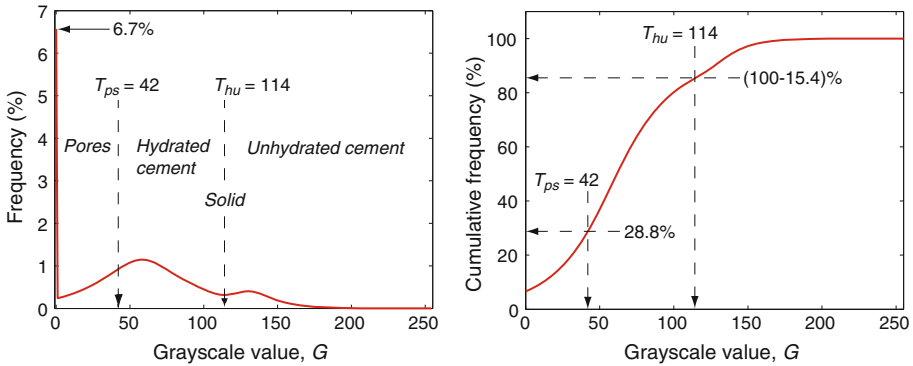


Fig. 2 Grayscale level frequency distribution (left) and cumulative distribution (right)

this plot, several distinct peaks are evident. First, approximately 6.7% of the voxels have a grayscale value of $G = 0$. This corresponds to air and water filled pores. Secondly, two peaks, at grayscale values of $G \simeq 60$ and $G \simeq 130$ are visible. These peaks are associated with hydrated and unhydrated cement, respectively.

On the basis of the distribution shown in Fig. 2, it could be argued that the pore/solid cut-off threshold should be set at a grayscale level of $G = 0$. This, however, leads to an unrealistically low porosity. Instead, the threshold can be determined to reproduce the desired porosity. For this purpose, the classic model of Powers (1962) may be used as suggested by Koster et al. (2006). This model includes the following predictions of volume fractions of capillary pores and unhydrated cement paste on the basis of the initial water/cement ratio and the current degree of hydration:

$$\phi_p = \frac{w/c - 0.36\alpha}{w/c + 0.32}, \quad \phi_u = \frac{0.32(1 - \alpha)}{w/c + 0.32}, \quad \phi_h + \phi_u + \phi_p = \phi_s + \phi_p = 1, \quad (1)$$

where w/c is the water/cement mass ratio, α is the degree of hydration, ϕ are the volume fractions with subscripts h, u, p and s referring to the hydrated, unhydrated, (capillary) pore and solid phases, respectively. In addition, the volume fraction of gel pores is given by $\phi_g = 0.19\alpha/(w/c + 0.32)$. However, these pores, which formally are considered part of the hydrated cement phase, do not contribute significantly to the mass transport and are therefore not considered in the following. On the basis of the expression for ϕ_u , the degree of hydration can be estimated. First, ϕ_u is estimated from the data by choosing a threshold of $G = T_{hu} = 114$, corresponding the lowest point in the valley between the two peaks (see Fig. 2). This gives a value of $\phi_u = 0.154$, leading to $\alpha = 0.63$. Finally, this degree of hydration, together with the water/cement ratio of $w/c = 0.45$ gives a porosity of $\phi_p = 0.290$. This porosity is realized (approximately) by a pore/solid phase threshold of $G = T_{ps} = 42$, giving a final porosity for the digitized sample of $\phi_p = 0.288$.

An example of a slice from the data set at this level of thresholding is shown in Fig. 3. From the individual slices, the full three-dimensional volume may be constructed. An example of a 64^3 volume extracted from the available 300^3 volume is shown in Fig. 4.

2.2 Microstructural Correlation Functions

A systematic approach to the characterization of random heterogeneous media by means of microstructural correlation functions has been described by Torquato (2002). Microstructural

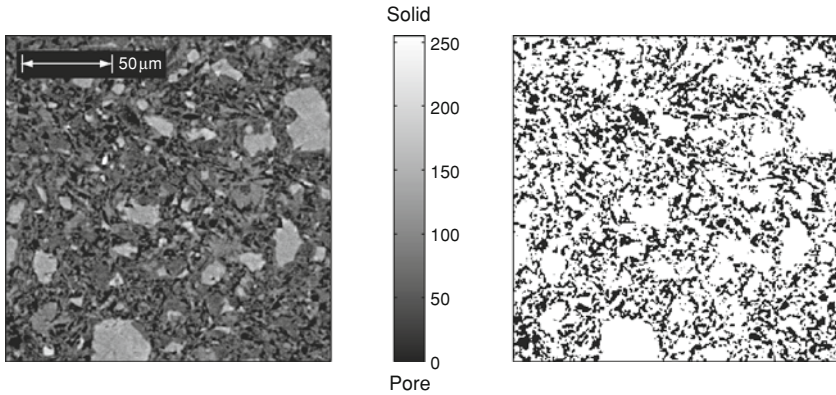


Fig. 3 Micro-CT slices of the cement paste at a resolution of $0.95 \mu\text{m}$. Each slice consists of 300×300 pixels. The *left* panel shows the original grayscale data and the *right* panel shows the result of thresholding at a grayscale level of 42

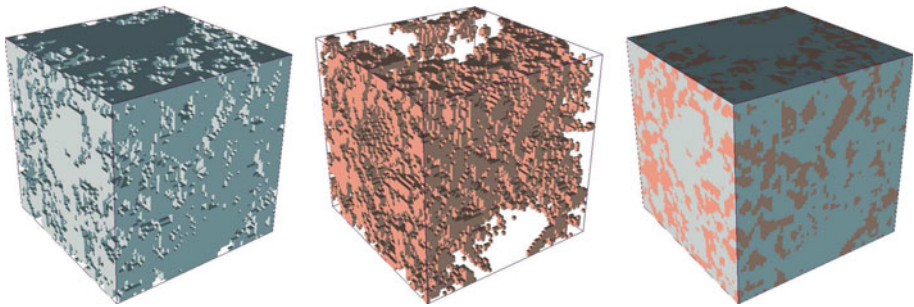


Fig. 4 Three-dimensional reconstruction of the cement paste: solid phase (*left*), pore space (*center*), and combined solid/pore phases (*right*). The volumes consist of $64^3 = 262,144$ voxels, each of which is represented by an 8-node finite element

correlation functions are useful both as a means of deriving rigorous bounds on the effective properties as well as to gain insights into the basic features of the material. In the following, we use two correlation functions for the latter purpose.

2.2.1 Two-Point Probability Function

Consider a material partitioned into two phases V_1 and V_2 . Introduce the indicator function for phase i :

$$\mathcal{I}^{(i)}(\mathbf{x}) = \begin{cases} 1, & \text{if } \mathbf{x} \in V_i, \\ 0, & \text{otherwise,} \end{cases} \tag{2}$$

where \mathbf{x} is the spatial coordinate. The probability of a point \mathbf{x} being contained within phase i is given by

$$\mathcal{P} \left\{ \mathcal{I}^{(i)}(\mathbf{x}) = 1 \right\} = \phi_i, \tag{3}$$

where ϕ_i is the phase fraction of the i th phase. The two-point probability function can now be defined as

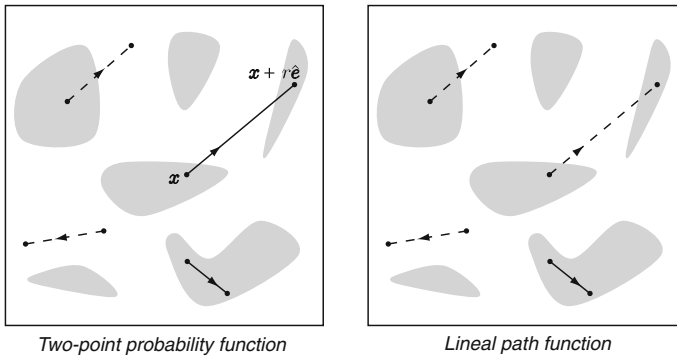


Fig. 5 Illustration of the two-point probability (*left*) and lineal-path (*right*) functions for the gray phase of the two-phase medium. Full segments indicate realizations that contribute to either function, while broken segments indicate realizations that do not

$$S_2^{(i)}(\mathbf{x}_1, \mathbf{x}_2) = \mathcal{P} \left\{ \mathcal{I}^{(i)}(\mathbf{x}_1) = 1 \wedge \mathcal{I}^{(i)}(\mathbf{x}_2) = 1 \right\}. \tag{4}$$

In other words, $S_2^{(i)}$ is the probability that two randomly chosen points \mathbf{x}_1 and \mathbf{x}_2 both are contained within phase i . For a statistically homogeneous material, S_2 is a function of the distance between \mathbf{x}_1 and \mathbf{x}_2 only. In this case, we have

$$S_2^{(i)}(r) = \mathcal{P} \left\{ \mathcal{I}^{(i)}(\mathbf{x}) = 1 \wedge \mathcal{I}^{(i)}(\mathbf{x} + r\hat{\mathbf{e}}) = 1 \right\}, \tag{5}$$

where \mathbf{x} is a randomly chosen point and $\hat{\mathbf{e}}$ is a random unit vector (see Fig. 5). A directional variant of this function can be defined as

$$S_{2\xi}^{(i)}(r) = \mathcal{P} \left\{ \mathcal{I}^{(i)}(\mathbf{x}) = 1 \wedge \mathcal{I}^{(i)}(\mathbf{x} + r\hat{\mathbf{e}}_\xi) = 1 \right\}, \tag{6}$$

where $\hat{\mathbf{e}}_\xi$ specifies some fixed direction, for example, along one of the coordinate axes.

2.2.2 Lineal-Path Function

The lineal-path function is similar to the two-point probability function, but counts only those realizations where the whole line segment (and not only its end points) is contained within phase i (see Fig. 5). We thus have

$$L^{(i)}(r) = \mathcal{P} \left\{ \mathcal{I}^{(i)}[\mathbf{x} + (1-s)r\hat{\mathbf{e}}] = 1, \forall s \in (0, 1) \right\}, \tag{7}$$

where $L^{(i)}$ is the lineal-path function for phase i . Again, a directional variant of this function can be defined as

$$L_\xi^{(i)}(r) = \mathcal{P} \left\{ \mathcal{I}^{(i)}[\mathbf{x} + (1-s)r\hat{\mathbf{e}}_\xi] = 1, \forall s \in (0, 1) \right\}. \tag{8}$$

We note that for $r = 0$, the two-point probability and lineal-path functions coincide and are equal to the phase fraction of the sampled phase.

2.2.3 Application to Cement Paste Data

The two-point probability and lineal-path functions were computed for the digitized cement paste using the procedure of [Yeong and Torquato \(1998\)](#). The results are shown in Fig. 6

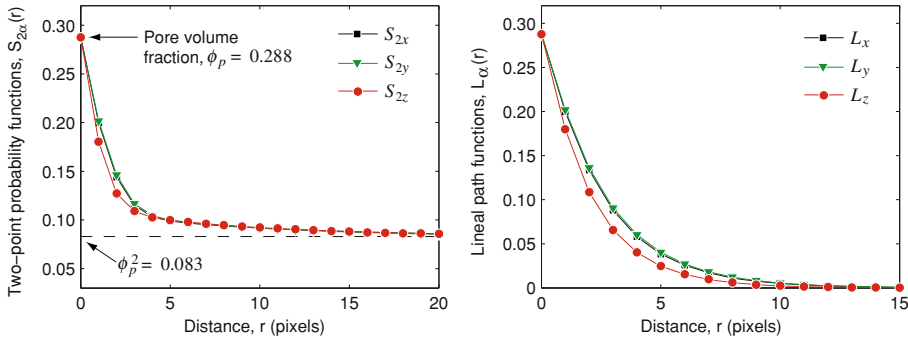


Fig. 6 Directional two-point probability (*left*) and lineal-path (*right*) functions for the pore phase of the cement paste (1 pixel \approx 1 μ m). Both functions reveal a slight anisotropy

where the x , y , and z directions refer to Fig. 1. Both functions display a slight anisotropy such that the microstructural characteristics in the x and y directions apparently differ slightly from those in the z direction. In view of the experimental procedure described in Sect. 2, such anisotropy can certainly be justified and it is rather gratifying that this subtle feature is captured in the XMT images.

The second point of note is that the correlation length is limited to some 20 pixels (corresponding to approximately 20 μ m). This suggests that the necessary size of the representative volume element may be of this order as well. In the following, this estimate will be confirmed by actual simulations.

3 Governing Equations and Homogenization Schemes

3.1 Local Equations

The types of diffusion phenomena considered in this article can be described by the classical diffusion equation. Conservation of mass is expressed by

$$\nabla \cdot \mathbf{j} = 0 \quad \text{in } V, \tag{9}$$

where \mathbf{j} is the mass flux. This flux is related to the concentration gradient by Fick’s law:

$$\mathbf{j} = -\mathbf{D}\nabla\psi \quad \text{in } V, \tag{10}$$

where ψ is the concentration of the diffusing species and \mathbf{D} is the diffusivity matrix. For a two-phase medium, this is given by

$$\mathbf{D} = \mathbf{D}(\mathbf{x}) = \mathbf{D}_1\mathcal{I}^{(1)}(\mathbf{x}) + \mathbf{D}_2\mathcal{I}^{(2)}(\mathbf{x}) \tag{11}$$

with \mathbf{D}_1 and \mathbf{D}_2 being the local diffusivities. In the general case, \mathbf{D}_1 and \mathbf{D}_2 are symmetric and positive semidefinite 3×3 matrix. For the present application of molecular diffusion in cement pastes, it is reasonable to assume that the diffusivity matrix is locally isotropic. We thus have

$$\mathbf{D}(\mathbf{x}) = \left[D_1\mathcal{I}^{(1)}(\mathbf{x}) + D_2\mathcal{I}^{(2)}(\mathbf{x}) \right] \mathbf{I}, \tag{12}$$

where \mathbf{I} is the unit matrix and D_1 and D_2 are the diffusivities of the two phases. Inserting (11) into (9) produces the classical diffusion equation

$$\nabla \cdot (\mathbf{D}\nabla\psi) = 0 \quad \text{in } V \tag{13}$$

which must be supplemented with appropriate boundary conditions.

For later reference, we also state the inverse of Fick’s law:

$$\mathbf{e} = \mathbf{S}\mathbf{j} \quad \text{in } V, \tag{14}$$

where \mathbf{S} is such that $\mathbf{D}\mathbf{S} = \mathbf{I}$, with \mathbf{I} being the unit matrix. The quantity \mathbf{e} can be thought of as the concentration gradient, cf. (10). This leads to the following alternative statement of the governing equations:

$$\begin{aligned} \nabla \times \mathbf{e} &= \mathbf{0} \quad \text{in } V, \\ \nabla \cdot \mathbf{j} &= \mathbf{0} \quad \text{in } V, \\ \mathbf{e} &= \mathbf{S}\mathbf{j} \quad \text{in } V, \end{aligned} \tag{15}$$

where the irrotational nature of \mathbf{e} implies the existence of a potential, ψ , such that $\mathbf{e} = -\nabla\psi$.

3.2 Homogenized Equations

Using standard arguments (see e.g. Whitaker 1998; Torquato 2002), the homogenized Fick’s law may be written as

$$\langle \mathbf{j} \rangle = -\mathbf{D}_{\text{eff}}\langle \mathbf{e} \rangle, \quad \langle \mathbf{e} \rangle = -\mathbf{S}_{\text{eff}}\langle \mathbf{j} \rangle \tag{16}$$

where $\langle \rho \rangle$ denotes the volume average of a quantity ρ :

$$\langle \rho \rangle = \frac{1}{V} \int_V \rho(\mathbf{x}) \, dV \tag{17}$$

and $\mathbf{D}_{\text{eff}} = \mathbf{S}_{\text{eff}}^{-1}$ is the effective diffusivity matrix. We note that this may display anisotropy even if the local phase diffusivities are isotropic.

It is the objective of any homogenization procedure to determine the effective diffusivity on the basis of the local properties and the microstructure of the material. In this context, it should be realized that the above effective moduli, strictly speaking, pertain only to infinite and statistically homogeneous media. That is, for a non-periodic, finite-size medium, it is generally not possible to define the concept of effective moduli in an unambiguous manner. Instead, the concept of effective moduli is replaced by the concept of apparent moduli which relate to specific boundary conditions. These moduli, resulting from the application of different boundary conditions, are related to each other via inequalities as summarized in the following sections.

3.3 Apparent Moduli—Single Realizations

Consider an arbitrary inhomogeneous medium of a finite size in the form of a unit cube. The medium is subjected to a homogeneous intensity field acting on its boundary S :

$$\mathbf{e} = \mathbf{e}_0 \quad \text{on } S \tag{18}$$

or, alternatively,

$$\phi = \mathbf{e}_0^T \mathbf{x} \quad \text{on } S, \tag{19}$$

where \mathbf{e}_0 is a specified intensity. We will refer to this as a Dirichlet boundary condition. For this particular type of homogenous intensity boundary condition, Hill’s condition is valid (see e.g. [Ostoja-Starzewski 2008](#)):

$$\langle \mathbf{j}^\top \mathbf{e} \rangle = \langle \mathbf{j} \rangle^\top \langle \mathbf{e} \rangle. \tag{20}$$

Fulfillment of this condition allows for two different, but equivalent, definitions of the effective modulus. For the type of Dirichlet boundary condition under consideration, these are the ‘direct’ definition:

$$\langle \mathbf{j} \rangle = \mathbf{D}_D \langle \mathbf{e} \rangle \tag{21}$$

and the ‘energetic’ definition:

$$\langle \mathbf{e}^\top \mathbf{D} \mathbf{e} \rangle = \langle \mathbf{e} \rangle^\top \mathbf{D}_D \langle \mathbf{e} \rangle. \tag{22}$$

In a similar manner, we may consider homogeneous flux, or Neumann, boundary conditions:

$$\mathbf{n}^\top \mathbf{j} = j_0 \text{ on } S, \tag{23}$$

where j_0 is a specified boundary flux. This boundary condition again implies fulfillment of Hill’s condition and we may define the associated effective modulus either as

$$\langle \mathbf{e} \rangle = \mathbf{S}_N \langle \mathbf{j} \rangle \tag{24}$$

or as

$$\langle \mathbf{j}^\top \mathbf{D} \mathbf{j} \rangle = \langle \mathbf{j} \rangle^\top \mathbf{D}_N \langle \mathbf{j} \rangle. \tag{25}$$

Finally, we consider the following mixed boundary conditions

$$\begin{aligned} \phi &= \phi_0 \text{ on } S_\xi^+ \\ \phi &= 0 \text{ on } S_\xi^- \\ \mathbf{n}^\top \mathbf{j} &= 0 \text{ on } S \setminus (S_\xi^+ \cup S_\xi^-) \end{aligned} \tag{26}$$

where S_ξ^+ and S_ξ^- are two opposite faces on the unit cube. This type of boundary condition is that typically employed in physical diffusion tests. Again, Hill’s condition is satisfied, and again the associated effective diffusivity may be defined as

$$\langle \mathbf{j} \rangle = \mathbf{D}_M \langle \mathbf{e} \rangle \tag{27}$$

or as

$$\langle \mathbf{e}^\top \mathbf{D} \mathbf{e} \rangle = \langle \mathbf{e} \rangle^\top \mathbf{D}_M \langle \mathbf{e} \rangle. \tag{28}$$

The three different moduli defined via the three different sets of boundary conditions can be shown to be related to each other via the following inequalities ([Huet 1990](#); [Jiang et al. 2002](#); [Ostoja-Starzewski 2008](#)):

$$\mathbf{S}_N^{-1} \preceq \mathbf{D}_M \preceq \mathbf{D}_D, \tag{29}$$

where \preceq denotes inequality in the semidefinite sense.¹ It should be noted that in the above, we have assumed that the unit cube problem is solved exactly for the given boundary condition, i.e. the flux field is divergence free and that the intensity field is irrotational. In actual

¹ For symmetric matrices $\mathbf{A} \in \mathbb{R}^{n \times n}$ and $\mathbf{B} \in \mathbb{R}^{n \times n}$, we have $\mathbf{A} \preceq \mathbf{B} \Leftrightarrow \mathbf{x}^\top (\mathbf{A} - \mathbf{B}) \mathbf{x} \leq 0 \forall \mathbf{x} \in \mathbb{R}^n$. Similarly, $\mathbf{A} \succeq \mathbf{B} \Leftrightarrow \mathbf{x}^\top (\mathbf{A} - \mathbf{B}) \mathbf{x} \geq 0 \forall \mathbf{x} \in \mathbb{R}^n$.

numerical calculations, at most one or the other requirement can be satisfied. In such cases, it is still possible to maintain inequalities of the above type provided that $\mathbf{D}_{\mathcal{N}}$ is computed on the basis of divergence free flux field and $\mathbf{D}_{\mathcal{D}}$ is computed on the basis of a rotation free intensity field.

3.4 Apparent Moduli—Stochastic Averages

Consider now the case where a single realization of a statistically homogeneous medium approaching the infinite volume limit is available. As detailed by [Ostoja-Starzewski \(2008\)](#), for such a medium it is possible to compute stochastic averages that fulfill bounds of the type (29). The procedure is as follows. From the infinite volume, a sufficiently large number of smaller volumes of a given finite size are extracted. Each such volume is then subjected to the boundary conditions of choice and the effective moduli are recorded. For a volume of a given size δ , we then have the following inequalities:

$$[\mathbf{S}_{\mathcal{N}}]_{\delta}^{-1} \leq \mathbf{D}_{\text{eff}} \leq [\mathbf{D}_{\mathcal{D}}]_{\delta} \tag{30}$$

and

$$[\mathbf{S}_{\mathcal{N}}]_{\delta}^{-1} \leq [\mathbf{D}_{\mathcal{M}}]_{\delta} \leq [\mathbf{D}_{\mathcal{D}}]_{\delta}, \tag{31}$$

where square brackets denote the arithmetic mean among the total number of volumes considered:

$$[\mathbf{A}]_{\delta} = \frac{1}{N} \sum_{i=1}^N \mathbf{A}_{\delta}^i \tag{32}$$

with \mathbf{A}_{δ}^i being the apparent moduli of the N volumes of size δ . Following, [Khisaeva and Ostoja-Starzewski \(2006\)](#), we will refer to such averages as *stochastic averages*. It should be noted that $[\mathbf{D}_{\mathcal{M}}]_{\delta}$ in general is not rigorously bounded, i.e. it may be both smaller than or larger than \mathbf{D}_{eff} . In practice, however, it is often observed that $[\mathbf{D}_{\mathcal{M}}]_{\delta}$ converges from above as δ is increased.

In the context of digitized media, it is quite natural to let the size δ denote the number of subdivisions on each side of a cube of volume δ^3 . In that case, the following chains of inequalities may be derived ([Jiang et al., 2002](#); [Ostoja-Starzewski, 2008](#)):

$$[\mathbf{S}_{\mathcal{N}}]_1^{-1} \leq [\mathbf{S}_{\mathcal{N}}]_2^{-1} \leq \dots \leq [\mathbf{S}_{\mathcal{N}}]_{2n}^{-1} \leq \dots \leq [\mathbf{S}_{\mathcal{N}}]_{\infty}^{-1} = \mathbf{D}_{\text{eff}} \tag{33}$$

$$[\mathbf{D}_{\mathcal{D}}]_1 \geq [\mathbf{D}_{\mathcal{D}}]_2 \geq \dots \geq [\mathbf{D}_{\mathcal{D}}]_{2n} \geq \dots \geq [\mathbf{D}_{\mathcal{D}}]_{\infty} = \mathbf{D}_{\text{eff}} \tag{34}$$

where $n \geq 1$ is an integer. We note here that $[\mathbf{S}_{\mathcal{N}}]_1^{-1}$ is equal to the Reuss lower bound on the effective diffusivity:

$$[\mathbf{S}_{\mathcal{N}}]_1^{-1} = (\phi_1 \mathbf{S}_1 + \phi_2 \mathbf{S}_2)^{-1} \leq \mathbf{D}_{\text{eff}} \tag{35}$$

while $[\mathbf{D}_{\mathcal{D}}]_1$ is equal to the Voigt upper bound:

$$[\mathbf{D}_{\mathcal{D}}]_1 = \phi_1 \mathbf{D}_1 + \phi_2 \mathbf{D}_2 \geq \mathbf{D}_{\text{eff}}. \tag{36}$$

In principle, the bounds (33)–(34) allow for a rigorous assessment of the effective properties of a heterogenous medium without having to consider the infinite volume limit and have been used in this spirit by [Ostoja-Starzewski and Schulte \(1996\)](#), [Pecullan et al. \(1999\)](#), [Jiang et al. \(2002\)](#), [Kanit et al. \(2003\)](#) and [Khisaeva and Ostoja-Starzewski \(2006\)](#) among others. However, these studies show that the practical value of the bounds is most pronounced in

the case where the phase properties are quite similar. That is, for large phase contrasts, the bounds cannot, in general, be expected to be particularly tight unless the considered volumes attain sizes that for practical numerical calculations are prohibitively large. For the problem at hand, where the phase contrast tends to infinity, preliminary tests have confirmed this general trend. In the following, we therefore choose to consider only the case of mixed boundary conditions. These have previously (for problems with moderate phase contrasts) been shown to provide considerably more accurate estimates of the effective properties than the Dirichlet and Neumann bounds (Jiang et al., 2002; Khisaeva and Ostoja-Starzewski, 2006). Furthermore, as noted by Ostoja-Starzewski (2006), in many cases, these boundary conditions are, in fact, those that best represent the conditions under which actual physical experiments are carried out. For diffusion tests, this is certainly the case, and the above mixed boundary conditions are exactly those that are used in almost all experimental setups.

4 Computational Homogenization Scheme

The computational procedure used for extracting effective transport follows that of a number of other authors, notably Zohdi and Wriggers (2001), Kanit et al. (2003) and Ostoja-Starzewski (2006). The basic procedure is as follows. A volume of a given size, δ , is first selected at random. The governing equations are then discretized over this volume by means of finite elements, and the apparent property is computed. For each δ , this procedure is repeated N times, where N is sufficiently large for the computed stochastic average to attain a constant value. Next, the volume size, δ , is increased, and the procedure is repeated until the stochastic average is deemed to be independent of the volume size. The final stochastic average is then taken as being the sought effective property.

4.1 Discretization of Boundary Value Problems

The discretization of the individual boundary value problems solved as part of the homogenization scheme employed follows standard finite element procedures. It is based on the following variational statement:

$$\begin{aligned}
 &\underset{\phi(\mathbf{x})}{\text{minimize}} && \frac{1}{2} \int_V \nabla \phi(\mathbf{x})^\top D(\mathbf{x}) \nabla \phi(\mathbf{x}) dV \\
 &\text{subject to} && \phi(\mathbf{x}) = \phi_0 \text{ on } S_\xi^+ \\
 &&& \phi(\mathbf{x}) = 0 \text{ on } S_\xi^-
 \end{aligned} \tag{37}$$

where the local diffusivity takes the form of a scalar, i.e. the local transport is assumed to be fully isotropic.

The primary variables, namely the concentrations, are approximated using shape functions that are continuous between the elements and continuous and differentiable within them. We thus have

$$\phi(\mathbf{x}) \approx N(\mathbf{x})\boldsymbol{\phi}^h \tag{38}$$

where N contains the shape functions and $\boldsymbol{\phi}^h$ are the nodal concentrations. Inserting these approximations into (37) and taking the boundary conditions into account, we have

$$\begin{aligned}
 &\underset{\boldsymbol{\phi}}{\text{minimize}} && \frac{1}{2} \boldsymbol{\phi}^\top K \boldsymbol{\phi} \\
 &\text{subject to} && A \boldsymbol{\phi} = \boldsymbol{\phi}_0,
 \end{aligned} \tag{39}$$

where ϕ is the global nodal variable vector, A and ϕ_0 specify the boundary conditions, $B = \nabla N$, and

$$K = \sum_{i=1}^{noel} \int_V B_i^T(x) D_i(x) B_i(x) dV \tag{40}$$

The problem (39) can eventually be reduced to solving a set of equations of the well-known type

$$K\phi = r \tag{41}$$

where r accounts for the boundary conditions and K has been modified to impose these boundary conditions. The discrete problems are constructed such that each voxel of XMT data coincides with an eight-node finite element with constant properties, corresponding to either the solid or the pore phase.

4.2 Computation of Apparent Moduli

The mixed boundary conditions used in this study allows for only three independent tests, corresponding to macroscopically one-dimensional flow in the x , y and z directions. This in turn allows for the determination of three independent transport coefficients. In the following, therefore, the macroscopic apparent diffusivity matrix is assumed to be of the type

$$D_{app} = \begin{bmatrix} D_{app}^x & & \\ & D_{app}^y & \\ & & D_{app}^z \end{bmatrix} \tag{42}$$

The three diffusion coefficients are determined from three independent 1D-type tests as described above, that is:

$$D_{app}^\xi = -\frac{\langle e_\xi(\mathbf{x}) \rangle}{\langle j_\xi(\mathbf{x}) \rangle}, \quad \xi = x, y, z. \tag{43}$$

Alternatively, and equivalently, the effective moduli may be determined directly on the basis of the boundary fluxes, corresponding to what is typically done in traditional physical laboratory tests.

4.3 Solution of Linear Equations

The overwhelming part of the computational effort is spent on solving the finite element equations (41). For this specific task, a modified version of the Itpack solver (Kincaid et al. 1982) has been developed. This solver, which is of the pre-conditioned conjugate gradient type, has the following approximate performance for the types of problems dealt within this study:

$$t_{cpu} \approx a \times n_{dof}^{1.24} = a \times \delta^{3.72} \tag{44}$$

where n_{dof} is the number of degrees-of-freedom, t_{cpu} is the cpu time and a is a machine-dependent constant. For a standard Dell laptop with a 2.3 GHz CPU, we have $a \approx 2 \times 10^{-6}$ s so that for $\delta = 32$ the total cpu time is of order 1 s, for $\delta = 64$ of order 10 s, and for $\delta = 128$ of order 2 min. It is worth noting that this performance is relatively insensitive to the conditioning of the equations due to smaller or larger phase contrasts. The solver, which will be detailed elsewhere, can be obtained from the corresponding author.

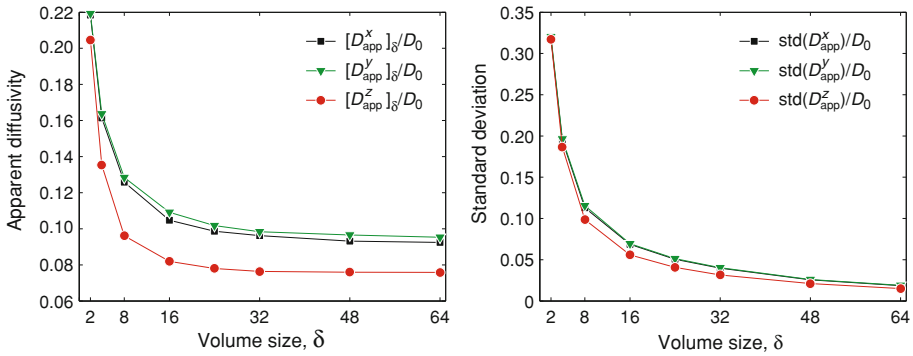


Fig. 7 Computed apparent diffusivities: stochastic averages (*left*) and standard deviations (*right*). The number of voxels (and hence finite elements) in each volume is given by δ^3

5 Numerical Results

In this section, the results of diffusion through the pore space of the cement paste are presented. Applying the computational homogenization procedure described in the previous section, the diffusivities shown in Fig. 7 are obtained. For each computed diffusivity, a total of 10,000 tests were performed. The diffusivity of the pore space was set equal to $D_0 = 1$ while the diffusivity of the solid phase, D_s , was set equal to an appropriately small, but non-zero, number. That is, we should satisfy $D_s/D_{\text{eff}} \approx 0$, while at the same time choosing D_s large enough to ensure a reasonable conditioning of the finite element equations. We have found that $D_s = 10^{-10}$ works well in this regard.

As seen from Fig. 7, the computed mean values appear to attain near-asymptotic values at around $\delta = 30$, while the standard deviation continues to decrease, though at a decreasing rate, as δ increases. The asymptotic values of the effective diffusion coefficients are:

$$\begin{aligned}
 D_{\text{eff}}^x &= [D_{\text{app}}^x]_{\infty} \approx [D_{\text{app}}^x]_{64} = 0.095 D_0 \\
 D_{\text{eff}}^y &= [D_{\text{app}}^y]_{\infty} \approx [D_{\text{app}}^y]_{64} = 0.095 D_0 \\
 D_{\text{eff}}^z &= [D_{\text{app}}^z]_{\infty} \approx [D_{\text{app}}^z]_{64} = 0.075 D_0
 \end{aligned}
 \tag{45}$$

Thus, the slight anisotropy suggested by the two-point probability and lineal-path functions (Fig. 5) manifests itself quite clearly with the diffusivity in the z -direction being somewhat smaller than in the x - and y -directions. This difference must necessarily be attributed to the sample preparation as described in Sect. 2, and although the general trend of a smaller diffusivity in the axial direction is entirely reasonable, the magnitude of this difference, $D_{\text{eff}}^x/D_{\text{eff}}^z = D_{\text{eff}}^y/D_{\text{eff}}^z = 1.27$, is perhaps somewhat surprising and certainly undesirable from an experimental point of view. Nevertheless, the results are consistent with the kind of anisotropy that could be expected from the ‘extrusion’ procedure used in the preparation of the samples.

The statistical distributions of the effective axial diffusivities for various volume sizes are shown in Fig. 8. We here observe that the computed diffusivities, above a certain value of δ , appear to be normally distributed within a relatively small tolerance. This result is somewhat surprising in that the transport properties of random porous media tend to follow right-skewed distributions such as the log-normal distribution (Chiles and Delfiner 1999).

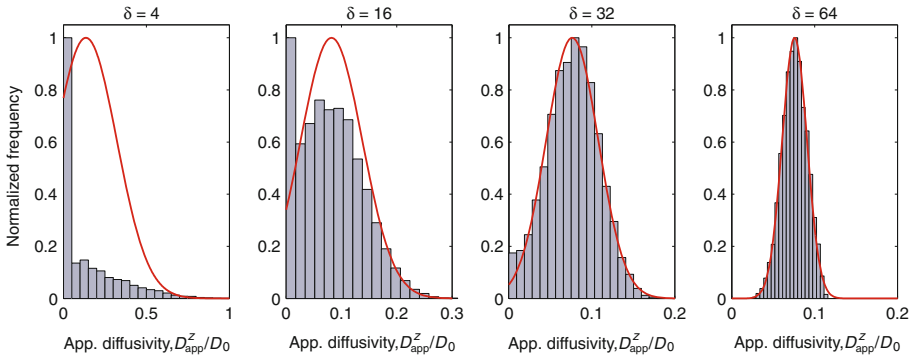


Fig. 8 Distribution of computed apparent axial diffusivities, D_{app}^z/D_0 , for various δ . The *full lines* represent Gaussian distributions obtained on the basis of the computed mean values and standard deviations

Indeed, such a distribution has been observed previously in the study of a different cement paste than the one considered here (Krabbenhoft et al. 2008).

Concerning the absolute magnitude of the effective diffusion coefficient, Garboczi and Bentz (1992) have proposed the following expression:

$$D_{eff}/D_0 = H(\phi_p - 0.18)1.8(\phi_p - 0.18)^2 + 0.07\phi_p^2 + 0.001 \tag{46}$$

where H is the Heaviside function. This formula is based on microstructural considerations and has been calibrated against experiments. By direct comparison to the above formula, we see that the computed effective diffusivities significantly overestimate what can be expected for a cement paste of the type considered. Indeed, for a cement paste with a porosity of around 29%, we should expect a value of $D_{eff}/D_0 \approx 0.028$, which is a factor of three to four less than obtained on the basis of the XMT images. The possible reasons for this deviation will be discussed in the following section.

6 Correction for Unresolved Submicron Features

The most immediate explanation for the deviation between computed and experimentally determined effective diffusivities is that the threshold level, $T_{ps} = 42$, is too high. We recall that this value was chosen on the basis of attaining a porosity of 29%. However, in principle, a small change in threshold level could reduce the effective diffusivity significantly without altering the porosity correspondingly. If, for example, the chosen pore/solid segmentation threshold implies a porosity close to the percolation threshold, a small change in T_{ps} would imply a potentially very large change in the effective diffusivity without affecting the porosity significantly. However, from Fig. 9, we see that this scenario is not responsible for the deviation between computed and experimental determined diffusivities. Thus, in order to achieve an effective diffusivity of $D_{eff}/D_0 \approx 0.028$, the threshold would have to be reduced to a level corresponding to < 20% porosity, which for the given water/cement ratio is unacceptably low.

The second hypothesis is based on the observation that of the total pore space, constituting 28.8% of the volume, only 6.7% is recognized as having a gray scale value of 0 (see Fig. 2). The remaining 22.1% is attributed to voxels with a grayscale value of up to 42. The most reasonable explanation for this failure to clearly identify the pore space is that the

Fig. 9 Effect of thresholding on porosity and computed effective diffusivities

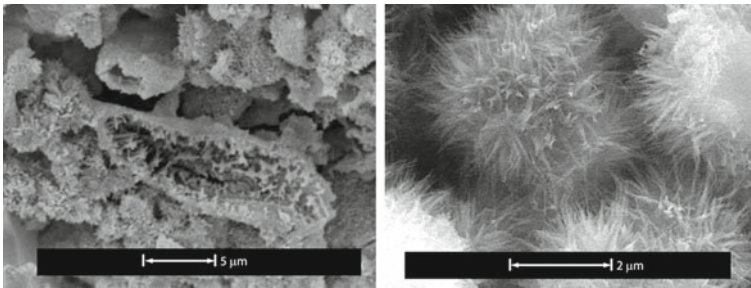
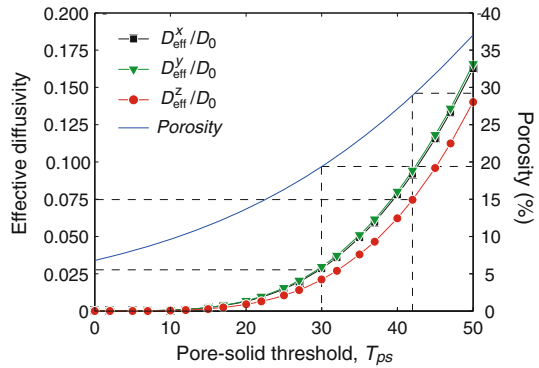


Fig. 10 Submicron structure of two different hydrated cement pastes. (Left) After Buenfeld (2007). (Right) After Tritthart and Häußler (2003)

resolution of the XMT scans ($\approx 1 \mu\text{m}$) is insufficient. Figure 10, which shows the submicron structure of two different hydrated cement pastes, offers some support of this hypothesis. From these figures, it appears that a resolution in the micrometer range is insufficient to capture the complex dendritic structures that form as a result of hydration. Moreover, this particular structure suggests that a voxel which has been identified as belonging to the pore space due to a low grayscale level in fact may contribute significantly to the effective resistance against diffusion. As such, assigning a constant diffusivity to the ‘pore space’ voxels may lead to significant overestimates of the effective diffusion coefficient.

Another indication that a significant part of the submicron features have not been resolved adequately comes in the form of the specific surface area of the XMT representations of the material. Following Torquato (2002), the specific surface area, s , may be calculated on the basis of the two-point probability function as

$$s = -\frac{1}{4} \left. \frac{dS_2}{dr} \right|_{r=0} \approx 3 \times 10^4 \text{ m}^2/\text{m}^3 \approx 0.02 \text{ m}^2/\text{g} \tag{47}$$

where we have assumed a cement paste density of $1.5 \text{ g}/\text{cm}^3$. This specific surface area is some three to four orders of magnitude lower than typical experimentally determined values (Barberon et al. 2003; Thomas et al. 1999), thus underlining the fact that significant submicron features have not been resolved adequately.

In an attempt to remedy this predicament, local diffusivities less than the free diffusivity were assigned to the intermediate gray scale voxels. This was done via a simple linear relationship so that the local pore diffusivities were taken as

Fig. 11 Computed effective diffusivities ($\delta = 64$) as function of linear grayscale diffusivity

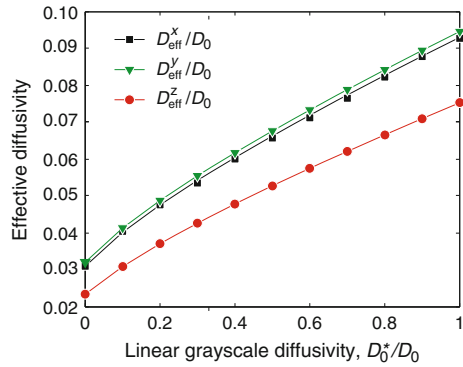
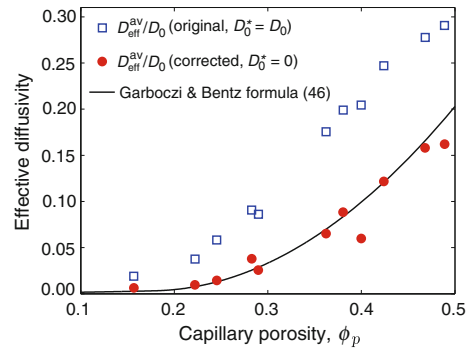


Fig. 12 Comparison between computed effective diffusivities and analytical estimate (46)



$$D_p/D_0 = 1 - (1 - D_0^*/D_0) \frac{G}{T_{ps}}, \quad 0 \leq G \leq T_{ps} \tag{48}$$

where D_p is the pore diffusivity, D_0 is the free diffusivity, D_0^* is a new constant that will be referred to as the ‘linear grayscale diffusivity’, G is the grayscale and T_{ps} is the pore/solid threshold. In other words, voxels with a grayscale count of 0 (6.7% in total) are assigned as the free diffusion coefficient, whereas the magnitude of the local diffusivities will decrease linearly to D_0^* at the pore/solid threshold. The computed effective diffusivities as function of the linear grayscale diffusivity, D_0^* , are shown in Fig. 11. From this figure, we see that a linear grayscale diffusivity of $D_0^* = 0$ apparently decreases the effective diffusion coefficients to a level around $D_{\text{eff}}/D_0 \approx 0.02\text{--}0.03$, which is roughly what should be expected for material considered.

In order to probe the validity of the proposed grayscale-pore diffusivity rule (48), we have analyzed a total of 12 different cement pastes as summarized in Table 1 and Fig. 12. Remarkably, for the most part, the diffusivities resulting from setting the linear grayscale diffusivity equal to zero, i.e. by letting the pore space diffusivity vary linearly with the grayscale value from $G = 0$ to $G = T_{ps}$, are in excellent agreement with the analytical/empirical formula (46) of Garboczi and Bentz (1992). It thus appears reasonable to conclude that the proposed empirical rule has general validity, at least for the cement pastes in the NIST data set. As for application to other data sets, the rule would probably in most cases furnish a reasonable first estimate.

The success of the proposed procedure for correcting for unresolved submicron features motivates the search for a more physical means of constructing such laws. From the wide

Table 1 Cement pastes analyzed

Dataset	w/c	T_{hu}	T_{ps}	α	ϕ_{p}	$D_{\text{eff}}^{\text{av}}/D_0$	$D_{\text{eff}}^{\text{av}}/D_0$	D_{eff}/D_0
						$D_0^* = D_0$	$D_0^* = 0$	Analyt. (46)
cez16_sld_2mmv1c300	0.40	151	48	0.805	0.157	0.0189	0.00641	0.00272
cez16_d_6dv1c300	0.40	112	39	0.696	0.222	0.0375	0.00953	0.00767
pt045_sld_2mmv1c300	0.45	142	53	0.745	0.245	0.0583	0.0145	0.0129
p35h40v1c300	0.35	117	49	0.462	0.283	0.0907	0.0378	0.0256
pt045_sld_7dv1c300	0.45	114	42	0.637	0.288	0.0832	0.0260	0.0278
p35h12v1c300	0.35	109	57	0.301	0.362	0.175	0.0651	0.0700
p35h08v1c300	0.35	106	48	0.260	0.381	0.198	0.0884	0.0836
p35h25v1c300	0.35	114	78	0.249	0.393	0.202	0.0513	0.0933
pate035_8_5dv1c300	0.35	143	102	0.244	0.400	0.204	0.0597	0.0992
pate03_1_7dv1c300	0.30	103	74	0.108	0.424	0.246	0.121	0.121
pt045_b_5dv2c300	0.40	99	58	0.181	0.468	0.277	0.158	0.166
pt045_h_5dv2c300	0.45	103	62	0.215	0.489	0.290	0.162	0.189

The data sets are from from <http://visiblecement.nist.gov>. The average effective diffusivities are calculated as the mean between the radial and longitudinal diffusivities (see Fig. 1): $D_{\text{eff}}^{\text{av}} = \frac{1}{2} \left[\frac{1}{2} (D_{\text{eff}}^{\text{x}} + D_{\text{eff}}^{\text{y}}) + D_{\text{eff}}^{\text{z}} \right]$. w/c = water/cement ratio, T_{hu} = hydrated/unhydrated cement threshold, T_{ps} = pore/solid threshold, α = estimated degree of hydration, ϕ_{p} = estimated porosity (see Sect. 2.1)

range of pastes considered (see Table 1), it appears that the rule in the present case is relatively insensitive to porosity, water/cement ration, hydration time, etc. We would, however, expect it to be a function of the particular type of cement paste (chemical composition of the cement, additives, etc.) and of the XMT settings (resolution, energy level, etc.). Ultimately, however, it could be envisioned that the submicron features actually are resolved. With recent advances in nano-CT, this could well be a reality in the near future. One would then use the effective nanoscale diffusivity as input to microscale models such as the ones considered in this article.

7 Conclusions

The problem of extracting effective diffusivities of cement pastes on the basis of X-ray microtomography images has been considered. A general computational homogenization framework is developed and applied to selected data sets. Additionally, the use of microstructural descriptors and statistical testing have been highlighted. With the resolution of the selected data sets ($\approx 1\mu\text{m}$), important submicron features are not resolved and it is necessary to perform a ‘correction’ to account for unresolved submicron features. This is done by ascribing the pore space a diffusivity less than the free diffusivity. In particular, it is found that a linear variation of the pore phase diffusivity with grayscale level furnishes reasonable results.

References

- Andrade, C.: Calculation of chloride diffusion coefficients in concrete from ionic migration measurements. *Cem. Concr. Res.* **23**, 724–742 (1993)

- Barberon, F., Korb, J.P., Petit, D., Morin, V., Bermejo, E.: Probing the surface area of a cement-based material by nuclear magnetic relaxation dispersion. *Phys. Rev. Lett.* **90**, 116103 (2003)
- Bentz, D.P. et al.: Microstructure and transport properties of porous building materials. II: Three-dimensional X-ray tomographic studies. *Mater. Struct.* **33**, 147–153 (2000)
- Bentz, D.P. et al.: The Visible cement data set. *J. Res. Natl. Inst. Stand. Technol.* **107**, 137–148 (2002) URL:<http://visiblecement.nist.gov>
- Buenfeld, N.: Concrete Durability Group. Secondary Electron Imaging. <http://www.concrete.cv.ic.ac.uk/durability> (2007)
- Chiles, J.P., Delfiner, P.: *Geostatistics, Modeling Spatial Uncertainty*. Wiley, New York (1999)
- Friedmann, H., Amiri, O., Ait-Mokhtar, A., Dumargue, P.: A direct method for determining chloride diffusion coefficient by using migration test. *Cem. Concr. Res.* **34**, 1967–1973 (2004)
- Garboczi, E.J., Bentz, D.P.: Computer simulation of the diffusivity of cement-based materials. *J. Mater. Sci.* **27**, 2083–2092 (1992)
- Huet, C.: Application of variational concepts to size effects in elastic heterogeneous bodies. *J. Mech. Phys. Solids* **38**, 813–841 (1990)
- Jiang, M., Jasiuk, I., Ostoja-Starzewski, M.: Apparent thermal conductivity of periodic two-dimensional composites. *Comput. Mater. Sci.* **25**, 329–338 (2002)
- Kanit, T., Forest, S., Galliet, I., Mounoury, V., Jeulin, D.: Determination of the size of the representative volume element for random composites: statistical and numerical approach. *Int. J. Solids Struct.* **40**, 3647–3679 (2003)
- Khisaeva, Z.F., Ostoja-Starzewski, M.: On the size of RVE in finite elasticity of random composites. *J. Elast.* **85**, 153–173 (2006)
- Kincaid, D.R., Respass, J.R., Young, D.M., Grimes, R.G.: Algorithm 586: ITPACK 2C: a FORTRAN package for solving large sparse linear systems by adaptive accelerated iterative methods. *ACM Trans. Math. Softw.* **8**, 302–322 (1982)
- Knackstedt, M.A. et al.: Elastic and transport properties of cellular solids derived from three-dimensional tomographic images. *Proc. R. Soc. A* **462**, 2833–2862 (2006)
- Koster, M., Hannawald, J., Brameshuber, W.: Simulation of water permeability and water vapor diffusion through hardened cement paste. *Comput. Mech.* **37**, 164–172 (2006)
- Krabbenhoft, K., Hain, M., Wriggers, P.: Computation of effective cement paste diffusivities from micro-tomographic images. In: Kompis, V. (ed.) *Composites with Micro- and Nano-Structure*, pp. 281–297. Spinger, Berlin (2008)
- Krabbenhoft, K., Krabbenhoft, J.: Application of the Poisson–Nernst–Planck equations to the migration test. *Cem. Concr. Res.* **38**, 77–88 (2008)
- Ostoj-Starzewski, M.: Material spatial randomness: From statistical to representative volume element. *Probab. Eng. Mech.* **21**, 112–132 (2006)
- Ostoj-Starzewski, M.: *Microstructural Randomness and Scaling in Mechanics of Materials*. Chapman & Hall/CRC, London/Boca Raton (2008)
- Ostoj-Starzewski, M., Schulte, J.: Bounding of effective thermal conductivities of multiscale materials by essential and natural boundary conditions. *Phys. Rev. B* **54**, 278–285 (1996)
- Pal, N.R., Pal, S.K.: A review on image segmentation techniques. *Pattern Recognit.* **26**, 1277–1294 (1993)
- Pecullan, S., Gibiansky, L.V., Torquato, S.: Scale effects on the elastic behavior of periodic and hierarchical two-dimensional composites. *J. Mech. Phys. Solids* **47**, 1509–1542 (1999)
- Powers, G.: Physical properties of cement paste. In: *Proceedings of the 4th international symposium on the chemistry of cement*, pp. 577–613 (1962)
- Promentilla, M.A.B., Sugiyama, T., Hitomi, T., Takeda, N.: Characterization of the 3D pore structure of hardened cement paste with synchrotron microtomography. *J. Adv. Concr. Technol.* **6**, 273–286 (2008)
- Promentilla, M.A.B., Sugiyama, T., Hitomi, T., Takeda, N.: Quantification of tortuosity in hardened cement pastes using synchrotron-based X-ray computed microtomography. *Cem. Concr. Res.* **39**, 548–557 (2009)
- Tang, L., Nilsson, L.O.: Rapid determination of the chloride diffusivity in concrete by applying an electric field. *Cem. Concr. Res.* **89**, 49–53 (1992)
- Thomas, J.J., Jennings, H.M., Allen, A.J.: The surface area of hardened cement paste as measured by various techniques. *Concr. Sci. Eng.* **1**, 45–64 (1999)
- Torquato, S.: *Random Heterogeneous Materials*. Springer, Berlin (2002)
- Trithart, J., Häußler, F.: Pore solution analysis of cement pastes and nanostructural investigations of hydrated C3S. *Cem. Concr. Res.* **33**, 1063–1070 (2003)
- Whitaker, S.: Coupled transport in multiphase systems: a theory of drying. *Adv. Heat Transf.* **31**, 1–102 (1998)
- Yeong, C.L.Y., Torquato, S.: Reconstructing random media. *Phys. Rev. E* **57**, 495 (1998)
- Zohdi, T.I., Wriggers, P.: Aspects of the computational testing of the mechanical properties of microheterogeneous material samples. *Int. J. Numer. Methods Eng.* **50**, 2573–2599 (2001)